Active Plasmonics and Active Chiral Plasmonics Through Orientation-Dependent Multipolar Interactions

Peter R. Stevenson,[†,(co)] Matthew Du,[‡,(co)] Charles Cherqui,[§] Marc R. Bourgeois,[§] Kate Rodriguez,[||] Jacob R. Neff,[†] Endora Abreu,[†] Ilse M. Meiler,[†] Venkata Ananth Tamma,[||] Vartkess Ara Apkarian,[||] George C. Schatz,[§] Joel Yuen-Zhou,[‡] and Jennifer S. Shumaker-Parry[,†]*

[†]Department of Chemistry, University of Utah, Salt Lake City, Utah 84112, USA

[‡]Department of Chemistry and Biochemistry, University of California San Diego, La Jolla, California 92093, USA

[§]Department of Chemistry, Northwestern University, Evanston, Illinois 60208, USA

[||]Department of Chemistry, University of California Irvine, Irvine, California 92697, USA

[(co)]Co-First Authors

*Email: shumaker-parry@chem.utah.edu

ABSTRACT

While most active plasmonic efforts focus on responsive metamaterials to modulate optical response, we present a simple alternative based on applied orientation control that can likely be implemented for many passive plasmonic materials. Passive plasmonic motifs are simpler to prepare but cannot be altered post-fabrication. We show that such systems can be easily manipulated through substrate orientation control to generate both active plasmonic and active chiral plasmonic responses. Using gold nanocrescents as our model platform, we demonstrate tuning of optical extinction from -21% to +36% at oblique incidence relative to normal incidence. Variation of substrate orientation in relation to incident polarization is also demonstrated to controllably switch chiroptical handedness (*e.g.*, $\Delta g = \pm 0.55$). These active plasmonic responses arise from the multipolar character of resonant modes. In particular, we correlate magnetoelectric and dipole-quadrupole polarizabilities with different light-matter orientation-dependence in both near- and far-field localized surface plasmon activity. Additionally, the attribution of far-field optical response to higher-order multipoles highlights the sensitivity offered by these orientation-dependent characterization techniques to probe the influence of localized electromagnetic field gradients on a plasmonic response. The sensitivity afforded by orientation-dependent optical characterization is further observed by the manifestation in both plasmon and chiral plasmon responses of unpredicted structural nanocrescent variance (i.e., left- and right-tip asymmetry) not physically resolved through topographical imaging.

KEYWORDS: active plasmonics, anisotropy, chiral plasmonics, extrinsic chirality, localized surface plasmon resonance, magnetoelectric effect

Controlled tuning of localized surface plasmon resonances (LSPRs) has been established as a powerful tool in light energy harvesting,[1] photochemical catalysis,[2, 3] photovoltaics,[4] photoluminescence,[5] chiral plasmonics,[6-10] assembly-triggered sensing,[11-15] as well as molecular[3, 16, 17] and chiral molecular[18, 19] detection. Pragmatically, the manipulation of LSPRs can be accomplished through the fabrication of structures with the desired range of geometric anisotropy.[20] However, typical nanostructures (particularly those resonant in the optical regime) are passive and cannot be reconfigured post-fabrication. Recently, considerable effort has focused on the advancement of active plasmonic[21-24] and active chiral plasmonic[25] systems, which offer the structural tunability to reversibly modify near-field LSPR behavior and associated far-field optical activity. Underlying mechanisms to control the behavior of such systems predominantly entail optical or physicochemical methods to change the electronic state of plasmonic materials or the refractive index of the embedding media.[22] Other methods include adjusting gap distances between constituent particles in the plasmonic entity.[22, 26] This latter approach also is the basis of similar strategies to control plasmonic chiroptical handedness through photoinduced structural reconfiguration (i.e., enantiomorphic switching from a left-handed to a right-handed design).[25, 27, 28] These exemplary active plasmonic approaches, however, remain intricate in fabrication and challenging to implement in practical applications that require control over broadband multimodal interactions.

As an alternative to the complex designs required for reconfigurable systems, we consider the extensive control over LSPR activity and associated far-field optical response achieved by exploiting light-matter orientation-dependence (LMOD) defined as the dependence between the orientation of a plasmonic structure and the polarization as well as angle of incidence of light in 3D space. Characterizing plasmonic LMOD can be considered analogous to methodologies

involving variable angle spectroscopy.[29, 30] For instance, when variable angle characterization is coupled with ellipsometry it can be a powerful tool in determining optical constants and deriving physical properties of both isotropic and anisotropic materials (*e.g.*, refractive indices, extinction coefficients, film thicknesses, film homogeneity, *etc.*).[31] The overall intent behind characterizing the LMOD of plasmonic systems supports the same general objective as variable angle spectroscopy—to further elucidate and define key optical properties of plasmonic materials.

The far-field response of each LSPR, consisting of displacement charges and currents sustained by a plasmonic structure, can be expressed in terms of a multipolar expansion about a point-scattering center, with leading contributions from electric dipole ($\boldsymbol{p}$), magnetic dipole ($\boldsymbol{m}$), and electric quadrupole ($\boldsymbol{Q}$) moments. Electric dipolar response dominates when the structure is small in comparison to the wavelength of light.[32] In this long-wave limit, the electromagnetic field is approximately constant throughout the structure and can be treated as electrostatic (i.e., a quasistatic approximation). On structures comparable in size to the wavelength of light, the phase of the electromagnetic field can vary substantially, and retardation effects cannot be ignored. In addition to modified plasmon wavelength and linewidths,[33-36] which increase with size for individual particles and oscillate with interparticle distance for coupled particles, retardation leads to a strengthened optical response of higher-order multipoles that can interact with field gradients:[37] $\boldsymbol{m}$ interacts with the curl of the electric field gradient (related to the magnetic field through Faraday's law), $\boldsymbol{Q}$ interacts with the symmetric part of the electric field gradient, and their cross-terms with $\boldsymbol{p}$ generate circular and linear dichroism, respectively.[38] Keeping within linear response, assuming a time-harmonic incident field, and showing terms up to first order in spatial dispersion, the constitutive equations of the induced electric and magnetic polarization can be expressed as (in Einstein notation)[39, 40]

$$p_i = A_{i,j}^{EE} E_j + A_{i,j}^{EH} H_j + A_{i,jk}^{EE} \nabla_k E_j + A_{i,jk}^{EH} \nabla_k H_j + \cdots \quad (1)$$

$$m_i = A_{i,j}^{HH} H_j + A_{i,j}^{HE} E_j + A_{i,jk}^{HE} \nabla_k E_j + A_{i,jk}^{HH} \nabla_k H_j + \cdots \quad (2)$$

where subscripts i, j, k denote Cartesian components, ∇ denotes spatial gradient of the incident electric (magnetic) field E_j (H_j), and the LSPR is characterized by the polarizability tensor A. In addition to isotropic electric (magnetic) polarizabilities $A_{i,j}^{EE}$ ($A_{i,j}^{HH}$), bi-anisotropic magnetoelectric induction is admitted through $A_{i,j}^{EH}$ and $A_{i,j}^{HE}$. The other polarizabilities shown—$A_{i,jk}^{EE}$, $A_{i,jk}^{EH}$, $A_{i,jk}^{HE}$, and $A_{i,jk}^{HH}$—allow for dipolar excitation through dipole-quadrupole coupling. The magnetic field gradients, which interact with magnetic quadrupole moments ($\boldsymbol{M}$), are included although $\boldsymbol{M}$ represents a multipole of the next order beyond magnetic dipole-electric quadrupole order.[40] Importantly, the transformation properties of the tensors associated with the different multipoles allow the orientation-dependent tuning of the optical response of a given LSPR.

For plasmonic nanostructures with structural anisotropy, the optical response is strongly dependent on the incidence angle and polarization. A prototypical example is a nanorod, which has dominant electric dipole polarizability along its long-axis:[41] the scattering intensity is high when the E-field polarization is parallel to the long-axis and low when perpendicular to it. Split-ring resonators, which sustain ring current and therefore magnetic dipole normal to the ring plane,[42] are prototypes that illustrate the profound effect of the angle of incidence on scattering response.[43] By tilting the angle of incidence away from normal, the handedness of a split-ring resonator chiroptical response can be switched between left and right owing to its dominant magnetoelectric dipolar coupling.[44] The polarizability terms $A_{i,j}^{EH}$ and $A_{i,j}^{HE}$, respectively, permit magnetic polarization induced by an applied electric field and vice versa.[45] Depending on the sign of the incidence angle, dipoles created by such "cross coupling" interfere with those created by "direct coupling" ($A_{i,j}^{EE}$ and $A_{i,j}^{HH}$), either constructively or destructively, producing an optical

response of one handedness or the other. As a result, LMOD can potentially endow traditionally *passive* plasmonic systems with the ability to elicit *active plasmonic* and *active chiral plasmonic* manipulation of LSPRs.

LMOD goes beyond conventional active plasmonics by offering opportunities to modify the orientation-dependence of the optical response based on the symmetries of the incident field. From Equations 1 and 2, it is evident excitation by field components of different orders ($\nabla^{\mathrm{n}}E, \nabla^{\mathrm{n}}H$) involves polarizabilities of distinct tensor ranks, each transforming uniquely under rotation. Thus, LMOD can be selectively expressed by appropriately shaping the spatial profile of the incident field.[46] For example, linear combinations of electromagnetic plane waves can be constructed to have larger field gradients allowing higher-order polarizabilities (tensor rank > 2) to dominate the optical response over dipole polarizabilities (tensor rank = 2).[47] Such a strategy is suitable for larger nanoparticles and systems of interacting nanoparticles for which higher-order multipoles become spectroscopically detectable.[48] Indeed, it has been theoretically shown for dolmen and nanodisk structures that polarizabilities describing dipole-quadrupole mixing can be on the same order of magnitude as dipole polarizabilities.[47] Dipole-quadrupole interferences are relevant to directional scattering[49] and emission[47, 50], which thus represent important applications of LMOD in nanophotonics.

In this report, we demonstrate active plasmonics and active chiral plasmonics through the orientation-dependent optical extinction of LSPRs in the far-field using gold (Au) nanocrescents (NCs) as the plasmonic platform. NCs sustain a progression of LSPRs, with electric and magnetic induction, similar to split-ring resonators.[51, 52] We show 3D substrate orientation alone allows for controllable and substantial tuning of LSPR modes in the near-field as well as extinction and chiroptical activity in the far-field. To identify the polarizabilities contributing to the observed

LMOD, we carry out measurements with systematic 3D rotations of the Au NCs and fit the optical responses with the generalized multipolar expansions of Equations 1 and 2. The extensive measurements of orientation-dependent extinction using plane polarized light (PPL) and circularly polarized light (CPL) allow a clear identification of dipolar, magnetoelectric, and dipole-quadrupole scattering components.

RESULTS AND DISCUSSION

Plasmonic Au NCs. A crescent structure is circularly curved with narrow antipodal tips that originate from a wider backbone region at the center of the structure. Crescents also exhibit one-fold rotational symmetry due to directional curvature. From a geometric perspective, crescents are mirror symmetric, which classifies them as achiral. As demonstrated in prior studies, plasmonic crescent structures exhibit a progression of biaxial multipole LSPRs over a broad spectral range when interrogated with PPL.[53-55] Recently, NCs also have been shown to generate giant extrinsic chiroptical activity with CPL.[56] The simple geometric anisotropy of plasmonic NCs as well as uniform size, shape, and orientation make them ideal for studying LMOD and the multipolar nature from which orientation-dependent optical response arises.

Au NCs, shown in the scanning electron microscopy (SEM) image in Figure 1a, were fabricated on a glass substrate using close-packed nanosphere template lithography (see Supporting Information and Figure S1 for the fabrication procedure).[53, 54, 57-59] This technique results in an array covering the entire substrate surface, comprised of uniformly oriented Au NCs. A color-scaled pixel frequency spectrum (Figure 1b) illustrates Fourier transform (FT) SEM image analysis of a 5,000 μm^2 substrate area at 4,000x magnification (the corresponding SEM micrograph is shown in Figure S2). As suggested by the symmetric circular pixel pattern, long-range periodicity

of the NC array persists while the hexagonal lattice becomes unordered at this range.[60] Short-range hexagonal lattice order appears to dissipate around 15,000x magnification, which represents a 600 μm^2 substrate area (Figure S3). As the spot size of our incident beam in optical characterization is a 1 cm^2 area, we anticipate no dominant contribution from short-range lattice order in ensemble measurements. Consequently, reported anisotropies are considered to arise primarily from Au NC geometry relative to the orientation and polarization of the incident light. This assumption is further supported by experimental assessment of diffraction effects as well as theoretical simulations discussed below.

The Au NCs implemented in the studies average 370 nm in length (tip-to-tip). Using atomic force microscopy (AFM), the maximum height was determined to be ~32 nm about their backbone (Figure 1c). This height reflects targeted fabrication conditions in depositing ~2 nm of a Cr adhesion layer and ~30 nm of Au. Since physical vapor deposition of fabrication metals occurs under continuous rotation, slightly offset from the metal source, a symmetric sloping from the thin, inner perimeter edge to the thicker backbone of the Au NC is observed in the line profile plots (Figure 1d). Likewise, from the central backbone region, the height tapers along both the width and length of the Au NC.

Near-Field Plasmon Anisotropy. The interpretation of far-field optical extinction activity is no trivial endeavor and can be further complicated by LMOD. While the constitutive relations in Equations 1 and 2 allow a completely empirical fitting of data and reconstruction of the effective point scattering multipoles, reconciliation of the terms with the extended near-field electric and magnetic polarizations associated with the LSPRs of the NCs is valuable. As such, to better conceptualize likely near-field distributions associated with Au NCs, we simulate the near-field spatial distributions associated with Au NC LSPRs using the finite-difference time-domain

(FDTD) method and compute the corresponding far-field extinction spectra associated with each LSPR mode. The simulations were performed using a three-dimensional model of a single Au NC on a dielectric glass substrate with geometric features emulating the fabricated structures in Figure 1 (compare Figure S4). The simulated and experimental extinction spectra for PPL excitation along the long- and short-axis of the crescent, at normal incidence, are shown in Figure 2. Despite the spectral shift between single NC simulation and the ensemble measurement, each resonance can be assigned by the comparison of extinction spectra in Figure 3 and are associated with the near-field electric and magnetic field enhancement maps presented in Figure 2. Figures 2a-c present field patterns upon illumination with PPL along the indicated directions (inset white arrows). In addition, we provide the field patterns obtained for excitation with left circularly polarized (LCP) light (Figures 2d-f), and right circularly polarized (RCP) light (Figures 2g-i). Experimental and simulated optical extinction spectra are compared in Figure 3. From this comparison, near-field resonance modes can be assigned to the experimental LSPR peaks.

With PPL oriented along the short-axis of the NC, the two dominant LSPR peaks at 590 nm and 1300 nm (Figure 3a) are respectively assigned—by comparing the simulated spectrum in Figure 3b—to the leading dipole mode along the backbone of the NC (Figure 2a) and the dipole mode producing maximum field enhancement at the tips (Figure 2b). With PPL oriented along the long-axis of the Au NC, three peaks appear at 550 nm, 1060 nm, and 2200 nm (Figure 3c) in good agreement with the simulation (Figure 3d). The resonance at 2200 nm corresponds to the fundamental dipole mode oscillating from tip-to-tip, and the curved path enforced by the NC structure generates the magnetic dipole normal to the plane, peaked in the inner curve (Figure 2c). The resonance at 550 nm corresponds to a quadrupole mode producing enhanced fields distributed along the backbone (Figure S5a), and the resonance at 1060 nm corresponds to a quadrupole mode

with enhanced fields primarily localized at the tips (Figure S5b). In summary, both near- and far-field LSPR activity under PPL excitation (Figures 2a-c) are clearly anisotropic relative to the incident light wavelength and polarization orientation.

Excitation with CPL illustrates an important principle, of near-field circular dichroism on an otherwise achiral structure. This is seen for the short-axis dipole mode (Figure 2b) that consists of two in-phase dipoles pointing from the backbone to the two tips. Shown in Figures 2e and h, the E-field intensity is larger on the top (bottom) tip using RCP (LCP). It appears that the top tip is right-handed, while the bottom tip is left-handed in this orientation. The effect arises from the retardation in the coupling between the displaced dipoles as the polarization angle sweeps the structure, and could in principle be observed through a near-field measurement, such as photo-induced force microscopy.[61] The effect at normal incidence disappears in the far-field, since the distributed response of the near-field can be collapsed into that of a point scattering center. It can be appreciated that upon tilting, the local anisotropy in polarization will generate orientation-dependent handedness in the far-field extinction (see discussion below).

Considering the above normal-incidence characterization of LMOD, the experimental studies presented in the remainder of this report predominantly focus on the LSPR modes at 590 nm, 1300 nm, and 2200 nm. These LSPRs will often be referred to using near-field modality designations (short-axis backbone dipole, short-axis tips dipole, and long-axis dipole, respectively) to connect to the predicted near-field activity as induced by the polarization of the incident light.

LMOD with PPL. Experimental LMOD is now assessed in comparison to normal incident light conditions. We use three angles (α, θ, ϕ) to specify NC orientation. Rotations by these angles are illustrated in Figure 4. In this diagram, the Au NC array and substrate surface are positioned at the optical axis where α, θ, $\phi = 0°$ (i.e., in the laboratory xy plane, with z-axis defined by the direction

of propagation of the incident light, as shown in Figure 4a and c). Establishment of the optical axis is discussed in the Supporting Information and depicted in Figure S6. Figure 4b illustrates selected in-plane orientations (ϕ) of the Au NC for α, θ = 0°. Rotations about the substrate normal, after tilting (α, $\theta \neq 0°$) are characterized by ϕ' (Figure 4c). Note ϕ' is defined for any out-of-plane orientation angle α, θ (i.e., positive or negative rotations).

To begin, the Au NC substrate was first positioned on the optical axis (compare Figure 4 and Figure S6) and rotated in ϕ under normal incidence, and optical extinction spectra were collected at 5° increments. Figure 5a shows a 3D polar surface plot of the spectra illustrating broadband, non-normalized optical extinction values from PPL. The long-axis dipole mode at 2200 nm appears at ϕ = 0° and 180°, while the short-axis tips dipole and short-axis backbone dipole (at 1300 nm and 590 nm, respectively) appears at ϕ = 90° and 270°. The response of these three dominant modes at normal incidence is further clarified in single-wavelength polar plots (Figures 5b-d).

To probe the LMOD of the optical response at non-normal incidence, the Au NC substrate was tilted from the optical axis to θ = 30° and characterized in ϕ' with fixed vertical PPL. Figure 5e shows the measured spectra as a 3D surface plot along with corresponding single-wavelength extinction 2D polar plots in Figures 5f-h. The Au NC substrate was then tilted to θ = -30° from the optical axis and characterized in the same fashion yielding a 3D polar surface plot (Figure 5i) with corresponding LSPR peak extinction polar plots (Figures 5j-l). Methodologically, the responses in Figure 5 represent conditions in which the light is *s*-polarized (transverse-electric) for each measurement. Figure 6 illustrates measurement conditions where the NC substrate is first rotated in α, θ, ϕ to a designated position away from the optical axis and then the PPL is rotated in ϕ (denoted by ϕ_{PPL}) about its propagation direction. Under this modified methodology, the

incident light fluctuates between *s*- or *p*-polarized (transverse-magnetic), where purely θ (α) rotation associated with appreciably more *p*-polarized light corresponds to the out-of-plane orientation associated with a maximum (minimum) intensity value in Figure 5. For comparison, normal incident responses are provided in Figure 6 and are equivalent, in principle, to those shown in Figure 5. By adjusting the plane of incidence to include different combinations of both *s*- and *p*-polarized light, additional dispersions in optical extinction intensity become accessible (as further suggested by Figures S6 and S7). For assistance in visualizing such *s*- and *p*-polarization conditions in relation to substrate rotation, Figure 4c shows the NC substrate rotated from the optical axis to θ = 30° in relation to the incident PPL. Overall, the orientation-dependent measurements presented above represent a previously unexplored strategy to manipulate LSPR optical extinction intensity. Utilizing this approach even allows for selective expression of overlapping peaks (*e.g.*, the short-axis backbone dipole at 590 nm and the long-axis backbone quadrupole at 550 nm).

LMOD of extinction intensity dispersions are clearly observed in Figures 5 and 6 for wavelengths associated with LSPR modes. Unexpectedly, both increases and decreases from the extinction values measured at normal incident light conditions are apparent in the polar plots. These responses demonstrate one prominent objective concerning active plasmonic approaches: the modulation of plasmonic optical intensity. In this case, however, the activity is observed from a passive array of Au NCs rather than a modulating array of plasmonic structures. For ease of comparison at each ϕ_{PPL}, intensity (I) changes are quantified by assessing $\Delta I/I_{max}$, where $\Delta I = I^{r'} - I^{r}$ and I_{max} is the maximum intensity. Here, r is the optical axis (α, θ, ϕ orientation discussed in Figure 4) set to 0°, 0°, 0° for the long-axis dipole resonance wavelength and 0°, 0°, 90° for the short-axis resonance wavelengths. The out-of-plane orientation is r' where in-plane

angle (ϕ' in Figure 4c) for NC orientation is equivalent to that of r (ϕ in Figure 4b). These $\Delta I/I_{max}$ values are reported in Table 1 and discussed in more detail below. Going beyond known biaxial LSPR responses, we have extended the optical extinction anisotropy involving plasmonic NCs to arbitrary orientations of the substrate and incident light.

To elucidate the origin of anisotropic LMOD, we fit Equations 1 and 2 to the Au NC optical extinction (see Methods Section).[62] This strategy assumes that the optical extinction of each Au NC LSPR can be represented by the polarizability tensor of a point-scattering center. Overall, the empirical fitting leads to satisfactory modeling of the experimental extinction under PPL (the black lines in Figures 5 and 6). The fitted polarizability tensor elements are represented in graphical (Figure 7) and tabular (Table S2) forms. The effect of individual terms on the extinction polar plots is illustrated in Figures S9-S13 of the Supporting Information. The additional sources of dipolar induction are necessary for modeling the experimentally observed LMOD of Au NC extinction. With isotropic dipole polarizabilities ($A_{i,i}^{EE}$, $A_{i,i}^{HH}$ in Equations 1 and 2), the observed LMOD at oblique incidence shown by the anisotropic extinction behavior in Figure 6 and Table 1 can be largely explained. For all three resonant wavelengths, decreases in extinction relative to normal incidence are mainly attributed to the reduction in the projection of the E-field on the induced electric dipole along either long- or short-axes of the Au NC (Figures S9b, S10b, and S12b). In contrast, increases in intensity with tilting at 590 and 1300 nm are mostly due to accessing the magnetic dipole polarizability oriented normal to the substrate plane (Figures S10d and S12d). The magnetic contribution originates from the curvature of the NC backbone, as in the archetypal split-ring resonators.[63] An exceptional case occurs for ϕ_{PPL} = 90° and 270° at θ = ±30° in Figure 6 where the intensity rise at 1300 nm is due to having significant electric dipole polarizability along

the Au NC height (Figure S11b), while the intensity reduction at 590 nm is associated with the lack thereof.

Excellent qualitative description of LMOD requires the inclusion of polarizabilities ($A_{i,jk}^{EE}$, $A_{i,jk}^{HH}$ in Equations 1 and 2) accounting for coupling between dipole and quadrupole (Figure 8b) of the same type (i.e., electric or magnetic). Notably, the change in extinction intensity at 590 nm is different when the substrate is rotated out-of-plane about the Au NC short-axis by either $\theta = \pm 30°$ (Figure 6 and Table 1). This lack of symmetry with respect to the sign of the out-of-plane angle is reproduced by polarizabilities representing interaction between z-dipole and zy-quadrupole, where both multipoles are either magnetic (Figure S12h) or electric (Figure S13d). While magnetic quadrupoles generally contribute insignificantly to optical response, their coupling to magnetic dipoles has been observed for U-shaped split-ring resonators tilted out-of-plane.[64] The importance of this interaction has also been suggested for individual resonators.[62] Table S3 summarizes the above and other anisotropic LMOD attributed to dipole-quadrupole coupling for the 590 nm LSPR. Polarizabilities capturing interactions between electric dipoles and quadrupoles also find relevance in the orientation-dependent optical response at 2200 nm (Figures 7a and S9e-f) and 1300 nm (Figures 7b and S10e-f). The broadband presence of dipole-quadrupole mixing is understandable given the size of analyzed particles (~370 nm) approaches those of the incident wavelengths (500 to 2500 nm).[47, 48] That these higher-order polarizabilities can be individually detected at all reveals the high sensitivity of the Au NCs to electromagnetic field gradients.

The proposed dipole-quadrupole couplings (Figure 8b) can also provide insight on geometric asymmetries of the Au NCs. First, consider the electric dipole along either NC long- or short-axis and the electric quadrupole spanning the plane containing this axis and the NC height. Their interaction at 2200 nm (Figure 7a) and 1300 nm (Figure 7b), according to symmetry-breaking

arguments, arises because the top and bottom of the Au NC are different. This result is consistent with specific structural features. From the AFM measurements, the NC short-axis length decreases from top to bottom of the nanoparticle (Figure 1d). Additionally, the Au NC resides on a dielectric substrate, which strengthens the multipolar response at the bottom of the nanostructure relative to the top (see near-field distributions reported by Bukasov *et al.*[58, 65, 66]). More intriguing is the interpretation of the p_z-Q_{zy} and m_z-M_{zy} couplings at 590 nm (Figure 7c). Following similar reasoning as above, these interactions imply a structural asymmetry between the left and right halves of the NC (each half contains a NC tip). In fact, electromagnetic simulations using the boundary element method (BEM) show that an idealized NC, created by taking the overlap region of two intersecting cylinders, yields several main features of the orientation-dependent extinction observed at 590 nm but not the subtle LMOD anisotropies (compare Figures S18b, f, and j with Figures 5b, f, and j and Table S3) and attributed dipole-quadrupole interactions. Though the left-right asymmetry is not readily apparent from the SEM and AFM imaging (Figure 1), its presence may result from the sample stage rotation and angles used during physical vapor deposition. Manifestation of such physical properties in the orientation-dependent extinction profiles would suggest remarkable sensitivity offered by this analytical technique, as the structural differences of the tips are below the resolution of our imaging capability.

Although the above arguments apply to individual Au NCs, we cannot fully dismiss interparticle scattering. This effect may help explain the minor disagreement between experimental data and analytical modeling (Figures 5 and 6). Validation of this hypothesis can be carried out, for example, by applying the point dipole theory developed by Koenderink and coworkers for plasmonic lattices.[67] The observable periodicity of the array in Figure 1b also suggests the possibility of long-range diffraction effects; however, none are experimentally observed

originating from the array *via* specular and diffuse transmission measurements at surface normal and non-normal incident light angles (see Supporting Information and Figure S8). The lack of detectable diffraction is likely due to an unordered lattice organization at longer ranges in the array, as is qualitatively illustrated in Figure 1b and Figure S3. Disparities between observed and modeled extinction intensities may also originate from the neglect of higher-order light-matter interactions (see Equations 1 and 2) and of higher-order multipoles (see Methods Section) in the empirical fitting.

Overall, the satisfactory agreement between experiment and analytical modeling validates the observed orientation dependence is that of the multipoles constituting the LSPRs. In particular, fitted polarizabilities representing dipole-quadrupole coupling are not only essential for reproducing the extinction measurements, but they can be traced to structural asymmetries of the Au NC substrate. The multipolar character also plays an important role in LMOD from excitation with CPL as discussed below.

LMOD with CPL. As previously discussed, the breaking of near-field symmetry by exciting LSPR activity *via* CPL (Figures 2d-i) presents an additional approach to manipulate plasmonic LMOD. Such symmetry breaking can be observed in the far-field as well. Although the NC geometry is achiral, plasmonic far-field handedness is known to manifest at out-of-plane incidence orientations. Termed extrinsic chirality,[68, 69] or pseudochirality in the context of bianisotropic composite media,[70] this phenomenon generally describes a planar achiral system that can be tilted relative to the incident CPL to generate chiroptical activity. Wang *et al.* have reported Au NCs can exhibit large circular dichroism (CD) when rotated out-of-plane.[56] Davis *et al.* also show the partitioning of orientation-dependent chiroptical response from misshapen aluminum crescent-like structures.[71] Here, we expound on such observations by measuring extinction dependency on in-

plane angle ϕ' for representative out-of-plane angles θ and provide additional insights on the extrinsic chirality of Au NCs are provided.

As expected from an achiral geometry, there is essentially no handedness at normal incidence in the far-field response (Figure 9a), although the near-field distribution induced by either LCP or RCP light is asymmetric (compare Figures 2d-i). Figures 9b-d show comparative polar CD profiles for the short-axis backbone dipole (590 nm), short-axis tips dipole (1300 nm), and long-axis dipole (2200 nm) generated at normal incidence. From the optical axis orientation, the substrate was rotated to θ = 30° and characterized in ϕ' with CPL. Figure 9e shows the compilation of these responses along with corresponding selected CD polar plots for the modes of interest in Figures 9f-h. The substrate was then tilted to θ = -30° from the optical axis and characterized in the same fashion yielding a 3D polar surface plot (Figure 9i) with corresponding single-wavelength CD polar plots for the modes of interest in Figures 9j-l.

At any of the three main resonance wavelengths, we observe dramatic sensitivity in the CD responses when out-of-plane angle θ is nonzero—not only with respect to Au NC in-plane orientation, but also with respect to whether θ is positive or negative. For either positive (Figures 9f-h) or negative (Figures 9j-l) out-of-plane angle, most prominent is the clear indication of two preferred in-plane orientations (ϕ' = 90° and 270°) to optimize chiroptical handedness, where each yields CD of equal magnitude but opposite signs. These orientations can be considered enantiomeric in response. Interestingly, positive and negative out-of-plane angles also constitute enantiomeric orientations, where the CD intensities (as a function of in-plane angle) are cardioid-like profiles for the short-axis backbone dipole facing opposite directions. Additional examination shows that for a given out-of-plane angle, these CD profiles are facing one direction at 590 nm (Figures 9b, f, and j) and 1300 nm (Figures 9c, g, and k) but another direction at 2200 nm (Figures

9d, h, and l). Therefore, the handedness of the optical response can be controlled not only by substrate orientation but also by incident wavelength. As discussed before, such tunability is a consequence of extrinsic chirality.[68, 69]

To further characterize the highly versatile manipulation of chiroptical handedness as illustrated in Figure 9, we calculate the anisotropy factor g. The g factor is the dimensionless ratio of extinction intensity (I) difference (i.e., in CD) to extinction intensity average for both circular polarizations:[72]

$$g = \frac{I_{LCP} - I_{RCP}}{\frac{1}{2}(I_{LCP} + I_{RCP})} \qquad (3)$$

This figure of merit normalizes the CD intensity to allow comparison of the chiroptical handedness associated with different experimental conditions. The g factors for the Au NCs at designated orientations are provided in Table 2. Spanning -0.55 to 0.55, such Au NC g factors are comparable to the huge values (i.e., $|g| \approx 0.26$ to 0.86) reported for intrinsically chiral nanohelices.[8, 73-75] A major advantage of extrinsic chirality, compared to intrinsic chirality, is the ability to simply switch CD handedness based on the manipulation of the substrate orientation relative to the incident ray. Here, we have demonstrated such facile switching of giant chiroptical activity illustrative of active chiral plasmonic behavior through LMOD.

To understand the orientation-dependence of observed g factors, we use the same modeling approach applied to extinction under PPL. Excellent fitting of the orientation-dependent CD is likewise obtained (Figure 9). The fitted polarizabilities (Figure 7) used to describe the chiroptical response represent magnetoelectric coupling (Figure 8a). Among the fitting parameters are those representing interaction between the electric dipole along the NC long-axis and magnetic dipole along the NC height ($A_{y,z}^{EH}$ and $A_{z,y}^{HE}$ in Equations 1 and 2). This coupling results in opposite signs for g factors corresponding to θ = ±30° and the same in-plane orientation (Table 2). More

generally, the dipolar interaction gives rise to the opposite facing cardioid-like CD profiles for positive and negative out-of-plane angles (Figures S14, S15, and S16a). In other words, dipolar magnetoelectric polarizabilities allow for a complete description of the orientation-dependent CD extinction at 1300 and 2220 nm.

In contrast, dipolar-quadrupolar magnetoelectric polarizabilities (namely $A_{i,jk}^{HE}$ in Equation 2) are needed to model salient features of the observed chiroptical activity at 590 nm and oblique incidence. Overall, positive CD values are smaller in magnitude than their negative counterparts (Figures 9f and j). A related observation is that, for fixed in-plane angles at ϕ' = 90° and 270°, the g factors are unequal for θ = ±30° (Table 2). Both results are successfully simulated by considering the polarizability representing interaction between the magnetic dipole, m_z, along the NC height and the yy electric quadrupole (Figure S16b). An even more prominent characteristic of the CD curves is the skewed cardioid-like profile, which is attributed to the magnetic dipole-electric quadrupole interaction between m_z and Q_{yx} (Figure S16c). The CPL-induced anisotropies discussed here are summarized in Table S3.

The identified magnetoelectric interactions are inherent to the ring-like structure of the Au NC. Excitation of the fundamental electric dipole propels clockwise or counterclockwise current along the NC backbone, thereby producing a magnetic dipole along the NC height (Figure 8a). The associated dependence of chiroptical handedness on the sign of the out-of-plane orientation has been observed in split-ring resonators.[44] Furthermore, the sign of each CD measurement is reproduced by electromagnetic BEM simulations (Figure S19f-h and j-l) of a Au NC that is uniform across its height (Figure S17). It follows that for any given substrate orientation, the relative handedness at the various resonance wavelengths likely arises from geometric features of a two-dimensional crescent. The dipole-quadrupole interaction between m_z and Q_{yx} can also be

explained with structural arguments: the backbone has greater height toward its back-end compared to its front-end (panel with green curve in Figure 1d). The two quadrupole lobes at the former location will be larger than those at the latter, resulting in an effective mode p_y that undergoes the aforementioned magnetoelectric dipolar coupling. Thus, the assumption of uniform NC height may explain why the BEM model does not yield the skewed cardioid-like CD profiles at 590 nm (Figures S19f and j). Future studies should verify our structure-based analyses of certain dipole-quadrupole couplings, as well as shed light on other such interactions revealed in this work.

CONCLUSIONS

We have shown controlled LMOD leads to substantial sculpting of near-field plasmon electric and magnetic activity. Most compelling, these observations illustrate simpler approaches toward both active plasmonic and active chiral plasmonic optical responses using a passive nanostructure motif. Suggested by FDTD simulations, near-field resonances can be selectively controlled simply by changing the polarization of the incident light (*e.g.*, PPL or CPL). The subsequent control of substrate orientation can further manipulate these more fundamental LSPR effects, producing dramatic changes in far-field optical properties attributed to near-field magnetoelectric dipolar and higher-order multipolar coupling effects. These interactions were identified by subtle anisotropies in extinction polar profiles, demonstrating LMOD can serve as visual fingerprints for multipolar interactions. Such trends, most evident for the short-axis backbone dipole mode, suggest plasmonic sensitivity to the applied field as well as its associated gradient field. As suggested by our analytical model, further studies pertaining to LMOD in relation to the geometry of a given nanostructure may yield improved sensitivity in the form of multipolar coupling events. It is anticipated these representative observations will influence the interpretation of optical scattering events in

plasmonic systems, as well as the principles of nanostructure design. Additionally, the magnetoelectric properties presented here suggest potential utility toward plasmon-based magnetic field sensors and plasmonic magnetoelectric scatterers based on our simple, orientation-dependent approach to elicit active plasmonic and active chiral plasmonic optical behavior.

METHODS

Nanofabrication Materials. Common glass microscope slides were used as optically transparent substrates for Au NCs. Polystyrene (PS) beads, with a 0.5 μm diameter at 0.4% w/w in water, for templating were purchased from Polysciences, Inc. An automated syringe pump from New Era Pump Systems, Inc. and a multichannel peristaltic pump from ISMATEC were used to form and deposit a close-packed colloidal monolayer of PS beads. Ultrapure water for surface substrate preparation and post-processing was purified to 18 MΩ using a Barnstead NANOpure diamond system. Removal of the sacrificial Cu layer was accomplished using concentrated H_2NO_3. Cu (99.999%), Cr (99.999%), and Au (99.99%) evaporation pellets were purchased from Kurt J. Lesker. Nanostructures were fabricated in an ISO 7 cleanroom using an Oxford 80 Plasmalab for reactive ion etching with oxygen plasma and a Denton SJ-20C for electron-beam evaporation of deposition metals. See Supporting Information for discussion of fabrication methods to prepare Au NCs.

Imaging Au Nanocrescents. SEM micrographs were obtained using a FEI Nova Nano630 SEM in immersion mode using a Helix detector. Atomic force micrographs were obtained using a Bruker Dimension Icon AFM with VeecoScanAsyst in contact mode.

Experimental Characterization. Optical extinction measurements with PPL and CPL were collected using a PerkinElmer Lambda 750 UV/Vis/NIR spectrophotometer. Spectra range in wavelength from 500 nm to 2500 nm (at 5 nm intervals) using a collimated beam size of 2 cm x

0.5 cm. A broadband linear polarizer, housed in an automated rotational drive accessory, was used to generate and control the orientation of PPL. Superachromatic quarter waveplates from Thorlabs were used to generate LCP and RCP light separately. These quarter waveplates were housed in indexing rotation mounts. A sample substrate holder comprised of a fine-tuned indexing rotation mount, fine-tuned base rotation mount, and goniometer (all from Thorlabs) was assembled using custom-machined aluminum adapters. Matlab was used to plot all experimental data. A custom script for 3D surface polar plots is accessible online at https://www.mathworks.com/matlabcentral/fileexchange/13200-3d-polar-plot. Experimental CD was calculated by subtracting $E_{LCP} - E_{RCP}$ where E is extinction (i.e., combined absorbed and forward scattered light) and multiplied by a factor of 32.98 to convert to units of degrees (conventional CD units as ellipticity).

Analytical Modeling. We consider an extended point-dipole formalism based on Equations 1 and 2 to calculate Au NC optical extinction from PPL and CPL.[62] This approach is appropriate when excited multipoles of higher order are too weak to contribute significantly to linear extinction. We treat the Au NC sample as an effective point scatterer whose polarizabilities incorporate the effects of the surrounding media.[47] Starting with Equations 1 and 2, stopping at quadrupolar contributions to the induced dipoles, and supposing plane-wave incident light with $\exp(i\boldsymbol{k}\cdot\boldsymbol{r})$ spatial dependence, we obtain for each LSPR

$$p_i = \left(A_{i,j}^{EE} + \frac{k_l}{k} A_{i,jl}^{EE}\right) E_j + \left(A_{ij}^{EH} + \frac{k_l}{k} A_{i,jl}^{EH}\right) H_j \qquad (4)$$

$$m_i = \left(A_{i,j}^{HE} + \frac{k_l}{k} A_{i,jl}^{HE}\right) E_j + \left(A_{i,j}^{HH} + \frac{k_l}{k} A_{i,jl}^{HH}\right) H_j \qquad (5)$$

where $k = |\boldsymbol{k}|$. Here and below, we have adopted the unit convention provided in Table S1. Under rotation, the polarizability terms $A_{i,j}$ and $A_{i,jl}$ transform as second- and third-rank tensors, while the electromagnetic field components transform as first-rank tensors (or vectors).[76] After

calculating dipoles with Equations 4 and 5, the associated extinction cross-section is computed using

$$\sigma_{\text{ext}} = \frac{C}{|E|^2} \text{Im}\left[\begin{pmatrix}\boldsymbol{E}\\ \boldsymbol{H}\end{pmatrix}^* \cdot \begin{pmatrix}\boldsymbol{p}\\ \boldsymbol{m}\end{pmatrix}\right] \qquad (6)$$

where C is a proportionality constant defined in the Supporting Information.[77, 78] To obtain values for the polarizability terms, least-squares fitting of Equations 4-6 is applied to experimental extinction measurements. This fitting is repeated for each of the three primary resonances focused on in this work. We note that spectral overlap between short-axis and long-axis modes, in particular the short-axis backbone dipole (590 nm) and the long-axis backbone quadrupole (550 nm), is accounted for by including terms for both modes.

All theoretical methods and calculations not presented here, or in the main text, are discussed in the Supporting Information. This discussion includes the FDTD and BEM calculations used throughout this work. In addition, the Supporting Information contains further discussion of the analytical model and fitting, as well as the numerical values of the polarizability contributions for each mode.

ASSOCIATED CONTENT

The Supporting Information is available free of charge on the ACS Publications website at DOI:

Au nanocrescent fabrication, Fourier transform SEM image analysis, near-field finite-difference time-domain calculations, establishment of an optical axis, specular and diffuse optical measurements, further discussion of analytical modeling, and boundary element method calculations (PDF)

AUTHOR INFORMATION

Corresponding Author

*Email: shumaker-parry@chem.utah.edu

Author Contributions

M.D. contributed equally with P.R.S. and is a co-first author for this paper. P.R.S, K.R., V.A.T., V.A.A., and J.S.S.P. designed the experimental research. P.R.S. fabricated nanocrescents, designed custom experimental equipment, analyzed experimental datasets, and interpreted all simulated and analytically modeled data. P.R.S., J.R.N., E.A., and I.M.M. carried out the experimental characterization. K.R., V.A.T., and V.A.A. assisted in preliminary modeling of reported LMOD and interpretation of experimental and analytically modeled results. M.D. and J.Y.Z. implemented the generalized multipole analytical model treatment of LMOD and overall interpretation of simulated data. C.C., M.R.B., and G.C.S. performed FDTD and BEM simulations. P.R.S., M.D., C.C., M.B., V.A.A, G.C.S., J.Y.Z., and J.S.S.P. wrote and edited the manuscript. All authors have given approval to the final version of the manuscript.

ACKNOWLEDGMENT

This work was primarily supported by NSF CaSTL CCI CHE 1414466 for P.R.S., C.C., K.R., J.R.N., E.A., I.M.M., V.A.T., V.A.A., G.C.S, and J.S.S.-P. involving experimental and theoretical applications. P.R.S. also acknowledges support from NSF MRSEC DMR 11-21252 for nanofabrication and associated characterization. The analytical modelling of orientation-dependent extinction, carried out by M.D. and J.Y.-Z., was supported by the US Department of Energy, Office of Science, Basic Energy Sciences, CPIMS Program under Early Career Research Program award DE-SC0019188. M.R.B. and G.C.S. acknowledge NSF CHE 1760537 for simulation theory development. This work made use of the University of Utah shared facilities of

the Micron Technology Foundation, Inc. Microscopy Suite sponsored by the College of Engineering, Health Sciences Center, Office of the Vice President for Research, and the Utah Science Technology and Research (USTAR) initiative of the State of Utah. This work was also performed in part at the Utah Nanofab sponsored by the College of Engineering, Office of the Vice President for Research, and the USTAR initiative of the State of Utah. P.R.S. also thanks Barry L. Stevenson for the custom Java program used to import and compile the many experimental data points collected for this study.

REFERENCES

1. Aslam, U.; Rao, V. G.; Chavez, S.; Linic, S., Catalytic Conversion of Solar to Chemical Energy on Plasmonic Metal Nanostructures. *Nat. Catal.* **2018,** *1*, 656-665.
2. Kale, M. J.; Avanesian, T.; Christopher, P., Direct Photocatalysis by Plasmonic Nanostructures. *ACS Catal.* **2014,** *4*, 116-128.
3. Zhan, C.; Chen, X.-J.; Yi, J.; Li, J.-F.; Wu, D.-Y.; Tian, Z.-Q., From Plasmon-Enhanced Molecular Spectroscopy to Plasmon-Mediated Chemical Reactions. *Nat. Rev. Chem.* **2018,** *2*, 216-230.
4. Standridge, S. D.; Schatz, G. C.; Hupp, J. T., Distance Dependence of Plasmon-Enhanced Photocurrent in Dye-Sensitized Solar Cells. *J. Am. Chem. Soc.* **2009,** *131*, 8407-8409.
5. Pachidis, P.; Cote, B. M.; Ferry, V. E., Tuning the Polarization and Directionality of Photoluminescence of Achiral Quantum Dot Films with Chiral Nanorod Dimer Arrays: Implications for Luminescent Applications. *ACS Appl. Nano Mater.* **2019,** *2*, 5681-5687.
6. Guerrero-Martínez, A.; Auguié, B.; Alonso-Gómez, J. L.; Džolić, Z.; Gómez-Graña, S.; Žinić, M.; Cid, M. M.; Liz-Marzán, L. M., Intense Optical Activity from Three-

Dimensional Chiral Ordering of Plasmonic Nanoantennas. *Angew. Chem. Int. Ed.* **2011,** *50*, 5499-5503.

7. Li, Z.; Zhu, Z.; Liu, W.; Zhou, Y.; Han, B.; Gao, Y.; Tang, Z., Reversible Plasmonic Circular Dichroism of Au Nanorod and DNA Assemblies. *J. Am. Chem. Soc.* **2012,** *134*, 3322-3325.
8. Song, C.; Blaber, M. G.; Zhao, G.; Zhang, P.; Fry, H. C.; Schatz, G. C.; Rosi, N. L., Tailorable Plasmonic Circular Dichroism Properties of Helical Nanoparticle Superstructures. *Nano Lett.* **2013,** *13*, 3256-3261.
9. Ma, W.; Kuang, H.; Wang, L.; Xu, L.; Chang, W.-S.; Zhang, H.; Sun, M.; Zhu, Y.; Zhao, Y.; Liu, L.; Xu, C.; Link, S.; Kotov, N. A., Chiral Plasmonics of Self-Assembled Nanorod Dimers. *Sci. Rep.* **2013,** *3*, 1934.
10. Ferry, V. E.; Smith, J. M.; Alivisatos, A. P., Symmetry Breaking in Tetrahedral Chiral Plasmonic Nanoparticle Assemblies. *ACS Photonics* **2014,** *1*, 1189-1196.
11. Jin, R.; Wu, G.; Li, Z.; Mirkin, C. A.; Schatz, G. C., What Controls the Melting Properties of DNA-Linked Gold Nanoparticle Assemblies? *J. Am. Chem. Soc.* **2003,** *125*, 1643-1654.
12. Fu, X.; Chen, L.; Li, J.; Lin, M.; You, H.; Wang, W., Label-Free Colorimetric Sensor for Ultrasensitive Detection of Heparin Based on Color Quenching of Gold Nanorods by Graphene Oxide. *Biosens. Bioelectron.* **2012,** *34*, 227-231.
13. Wang, J.; Zhang, P.; Li, C. M.; Li, Y. F.; Huang, C. Z., A Highly Selective and Colorimetric Assay of Lysine by Molecular-Driven Gold Nanorods Assembly. *Biosens. Bioelectron.* **2012,** *34*, 197-201.

14. Placido, T.; Aragay, G.; Pons, J.; Comparelli, R.; Curri, M. L.; Merkoçi, A., Ion-Directed Assembly of Gold Nanorods: A Strategy for Mercury Detection. *ACS Appl. Mater. Interfaces* **2013,** *5*, 1084-1092.

15. Ross, M. B.; Ashley, M. J.; Schmucker, A. L.; Singamaneni, S.; Naik, R. R.; Schatz, G. C.; Mirkin, C. A., Structure-Function Relationships for Surface-Enhanced Raman Spectroscopy-Active Plasmonic Paper. *J. Phys. Chem. C* **2016,** *120*, 20789-20797.

16. Xin, H.; Namgung, B.; Lee, L. P., Nanoplasmonic Optical Antennas For life Sciences and Medicine. *Nat. Rev. Mater.* **2018,** *3*, 228-243.

17. Langer, J.; Jimenez de Aberasturi, D.; Aizpurua, J.; Alvarez-Puebla, R. A.; Auguie, B.; Baumberg, J. J.; Bazan, G. C.; Bell, S. E. J.; Boisen, A.; Brolo, A. G.; Choo, J.; Cialla-May, D.; Deckert, V.; Fabris, L.; Faulds, K.; Garcia de Abajo, F. J.; Goodacre, R.; Graham, D.; Haes, A. J.; Haynes, C. L.*, et al.*, Present and Future of Surface-Enhanced Raman Scattering. *ACS Nano* **2020,** *14*, 28-117.

18. Ma, W.; Kuang, H.; Xu, L.; Ding, L.; Xu, C.; Wang, L.; Kotov, N. A., Attomolar DNA Detection with Chiral Nanorod Assemblies. *Nat. Commun.* **2013,** *4*, 2689.

19. Zhao, Y.; Askarpour, A. N.; Sun, L.; Shi, J.; Li, X.; Alù, A., Chirality Detection of Enantiomers Using Twisted Optical Metamaterials. *Nat. Commun.* **2017,** *8*, 14180.

20. Thorkelsson, K.; Bai, P.; Xu, T., Self-Assembly and Applications of Anisotropic Nanomaterials. *Nano Today* **2015,** *10*, 48-66.

21. Yang, A.; Hryn, A. J.; Bourgeois, M. R.; Lee, W.-K.; Hu, J.; Schatz, G. C.; Odom, T. W., Programmable and Reversible Plasmon Mode Engineering. *Proc. Natl. Acad. Sci. U. S. A.* **2016,** *113*, 14201-14206.

22. Jiang, N.; Zhuo, X.; Wang, J., Active Plasmonics: Principles, Structures, and Applications. *Chem. Rev.* **2018,** *118*, 3054-3099.

23. Wang, D.; Wang, W.; Knudson, M. P.; Schatz, G. C.; Odom, T. W., Structural Engineering in Plasmon Nanolasers. *Chem. Rev.* **2018,** *118*, 2865-2881.

24. Zheng, C. Y.; Palacios, E.; Zhou, W.; Hadibrata, W.; Sun, L.; Huang, Z.; Schatz, G. C.; Aydin, K.; Mirkin, C. A., Tunable Fluorescence from Dye-Modified DNA-Assembled Plasmonic Nanocube Arrays. *Adv. Mater. (Weinheim, Ger.)* **2019,** *31*, 1904448.

25. Hentschel, M.; Schäferling, M.; Duan, X.; Giessen, H.; Liu, N., Chiral Plasmonics. *Sci. Adv.* **2017,** *3*, e1602735.

26. Liu, N.; Guo, H.; Fu, L.; Kaiser, S.; Schweizer, H.; Giessen, H., Three-Dimensional Photonic Metamaterials at Optical Frequencies. *Nat. Mater.* **2007,** *7*, 31.

27. Zhang, S.; Zhou, J.; Park, Y.-S.; Rho, J.; Singh, R.; Nam, S.; Azad, A. K.; Chen, H.-T.; Yin, X.; Taylor, A. J.; Zhang, X., Photoinduced Handedness Switching in Terahertz Chiral Metamolecules. *Nat. Commun.* **2012,** *3*, 942.

28. Wang, S.; Zhang, Y.; Qin, X.; Zhang, L.; Zhang, Z.; Lu, W.; Liu, M., Guanosine Assembly Enabled Gold Nanorods with Dual Thermo- and Photoswitchable Plasmonic Chiroptical Activity. *ACS Nano* **2020**.

29. Woollam, J. A.; Johs, B.; Herzinger, C. M.; Hilfiker, J.; Synowicki, R.; Bungay, C. L., Overview of Variable Angle Spectroscopic Ellipsometry (Vase), Part I: Basic Theory and Typical Applications. *Crit. Rev. Opt. Sci. Technol.* **1999,** *CR72*, 3-28.

30. Johs, B.; Woollam, J. A.; Herzinger, C. M.; Hilfiker, J.; Synowicki, R.; Bungay, C. L., Overview of Variable Angle Spectroscopic Ellipsometry (Vase), Part Ii: Advanced Applications. *Crit. Rev. Opt. Sci. Technol.* **1999,** *CR72*, 29-58.

31. Woollam, J. A.; Snyder, P. G., Fundamentals and Applications of Variable Angle Spectroscopic Ellipsometry. *Mater. Sci. Eng., B* **1990,** *B5*, 279-283.

32. Bourgeois, M. R.; Liu, A. T.; Ross, M. B.; Berlin, J. M.; Schatz, G. C., Self-Assembled Plasmonic Metamolecules Exhibiting Tunable Magnetic Response at Optical Frequencies. *J. Phys. Chem. C* **2017,** *121*, 15915-15921.

33. Maier, S. A., *Plasmonics: Fundamentals and Applications*. Springer Science & Business Media: 2007.

34. Dahmen, C.; Schmidt, B.; von Plessen, G., Radiation Damping in Metal Nanoparticle Pairs. *Nano Lett.* **2007,** *7*, 318-322.

35. Olk, P.; Renger, J.; Wenzel, M. T.; Eng, L. M., Distance Dependent Spectral Tuning of Two Coupled Metal Nanoparticles. *Nano Lett.* **2008,** *8*, 1174-1178.

36. Taubert, R.; Ameling, R.; Weiss, T.; Christ, A.; Giessen, H., From near-Field to Far-Field Coupling in the Third Dimension: Retarded Interaction of Particle Plasmons. *Nano Lett.* **2011,** *11*, 4421-4424.

37. Myroshnychenko, V.; Rodriguez-Fernandez, J.; Pastoriza-Santos, I.; Funston, A. M.; Novo, C.; Mulvaney, P.; Liz-Marzan, L. M.; De Abajo, F. J. G., Modelling the Optical Response of Gold Nanoparticles. *Chem. Soc. Rev.* **2008,** *37*, 1792-1805.

38. Banik, M.; Rodriguez, K.; Hulkko, E.; Apkarian, V. A., Orientation-Dependent Handedness of Chiral Plasmons on Nanosphere Dimers: How to Turn a Right Hand into a Left Hand. *ACS Photonics* **2016,** *3*, 2482-2489.

39. Barron, L. D., *Molecular Light Scattering and Optical Activity*. 2 ed.; Cambridge University Press: Cambridge, England, 2004.

40. Raab, R. E.; de Lange, O. L., *Multipole Theory in Electromagnetism: Classical, Quantum, and Symmetry Aspects, with Applications*. Oxford University Press on Demand: 2005; Vol. 128, p 248.

41. Sönnichsen, C.; Franzl, T.; Wilk, T.; von Plessen, G.; Feldmann, J.; Wilson, O.; Mulvaney, P., Drastic Reduction of Plasmon Damping in Gold Nanorods. *Phys. Rev. Lett.* **2002,** *88*, 077402.

42. Banzer, P.; Peschel, U.; Quabis, S.; Leuchs, G., On the Experimental Investigation of the Electric and Magnetic Response of a Single Nano-Structure. *Opt. Express* **2010,** *18*, 10905-10923.

43. Baumberg, J. J.; Kelf, T. A.; Sugawara, Y.; Cintra, S.; Abdelsalam, M. E.; Bartlett, P. N.; Russell, A. E., Angle-Resolved Surface-Enhanced Raman Scattering on Metallic Nanostructured Plasmonic Crystals. *Nano Lett.* **2005,** *5*, 2262-2267.

44. Sersic, I.; van de Haar, M. A.; Arango, F. B.; Koenderink, A. F., Ubiquity of Optical Activity in Planar Metamaterial Scatterers. *Phys. Rev. Lett.* **2012,** *108*, 223903.

45. Ross, M. B.; Bourgeois, M. R.; Mirkin, C. A.; Schatz, G. C., Magneto-Optical Response of Cobalt Interacting with Plasmonic Nanoparticle Superlattices. *J. Phys. Chem. Lett.* **2016,** *7*, 4732-4738.

46. Zambrana-Puyalto, X.; Vidal, X.; Molina-Terriza, G., Excitation of Single Multipolar Modes with Engineered Cylindrically Symmetric Fields. *Opt. Express* **2012,** *20*, 24536-24544.

47. Bernal Arango, F.; Coenen, T.; Koenderink, A. F., Underpinning Hybridization Intuition for Complex Nanoantennas by Magnetoelectric Quadrupolar Polarizability Retrieval. *ACS Photonics* **2014,** *1*, 444-453.

48. Myroshnychenko, V.; Rodríguez-Fernández, J.; Pastoriza-Santos, I.; Funston, A. M.; Novo, C.; Mulvaney, P.; Liz-Marzán, L. M.; García de Abajo, F. J., Modelling the Optical Response of Gold Nanoparticles. *Chem. Soc. Rev.* **2008,** *37*, 1792-1805.

49. Babicheva, V. E.; Evlyukhin, A. B., Metasurfaces with Electric Quadrupole and Magnetic Dipole Resonant Coupling. *ACS Photonics* **2018,** *5*, 2022-2033.

50. Hancu, I. M.; Curto, A. G.; Castro-López, M.; Kuttge, M.; van Hulst, N. F., Multipolar Interference for Directed Light Emission. *Nano Lett.* **2014,** *14*, 166-171.

51. Okamoto, T.; Fukuta, T.; Sato, S.; Haraguchi, M.; Fukui, M., Visible Near-Infrared Light Scattering of Single Silver Split-Ring Structure Made by Nanosphere Lithography. *Opt. Express* **2011,** *19*, 7068-7076.

52. Okamoto, T.; Otsuka, T.; Sato, S.; Fukuta, T.; Haraguchi, M., Dependence of Lc Resonance Wavelength on Size of Silver Split-Ring Resonator Fabricated by Nanosphere Lithography. *Opt. Express* **2012,** *20*, 24059-24067.

53. Cooper, C. T.; Rodriguez, M.; Blair, S.; Shumaker-Parry, J. S., Polarization Anisotropy of Multiple Localized Plasmon Resonance Modes in Noble Metal Nanocrescents. *J. Phys. Chem. C* **2014,** *118*, 1167-1173.

54. Cooper, C. T.; Rodriguez, M.; Blair, S.; Shumaker-Parry, J. S., Mid-Infrared Localized Plasmons through Structural Control of Gold and Silver Nanocrescents. *J. Phys. Chem. C* **2015,** *119*, 11826-11832.

55. Swartz, M.; Rodriguez, M.; Quast, A. D.; Cooper, C. T.; Blair, S.; Shumaker-Parry, J. S., Aluminum Nanocrescent Plasmonic Antennas Fabricated by Copper Mask Nanosphere Template Lithography. *J. Phys. Chem. C* **2016,** *120*, 20597-20603.

56. Wang, Y.; Qi, J.; Pan, C.; Wu, Q.; Yao, J.; Chen, Z.; Chen, J.; Li, Y.; Yu, X.; Sun, Q.; Xu, J., Giant Circular Dichroism of Large-Area Extrinsic Chiral Metal Nanocrecents. *Sci. Rep.* **2018,** *8*, 3351.

57. Shumaker-Parry, J. S.; Rochholz, H.; Kreiter, M., Fabrication of Crescent-Shaped Optical Antennas. *Adv. Mater.* **2005,** *17*, 2131-2134.

58. Bukasov, R.; Ali, T. A.; Nordlander, P.; Shumaker-Parry, J. S., Probing the Plasmonic near-Field of Gold Nanocrescent Antennas. *ACS Nano* **2010,** *4*, 6639-6650.

59. Swartz, M. M. Fabrication and Characterization of Al and Mg Nanoparticles. Doctoral Dissertation, University of Utah, Salt Lake City, Utah, USA, August 22, 2017.

60. Feixas, M., *Information Theory Tools for Image Processing*. Morgan & Claypool Publishers: San Rafael, CA, 2014.

61. Rajaei, M.; Almajhadi, M. A.; Zeng, J.; Wickramasinghe, H. K., Near-Field Nanoprobing Using Si Tip-Au Nanoparticle Photoinduced Force Microscopy with 120: 1 Signal-To-Noise Ratio, Sub-6-Nm Resolution. *Opt. Express* **2018,** *26*, 26365-26376.

62. Varault, S.; Rolly, B.; Boudarham, G.; Demésy, G.; Stout, B.; Bonod, N., Multipolar Effects on the Dipolar Polarizability of Magneto-Electric Antennas. *Opt. Express* **2013,** *21*, 16444-16454.

63. García-García, J.; Martín, F.; Baena, J. D.; Marqués, R.; Jelinek, L., On the Resonances and Polarizabilities of Split Ring Resonators. *J. Appl. Phys.* **2005,** *98*, 033103.

64. Wu Pin, C.; Chen Wei, T.; Yang, K.-Y.; Hsiao Chih, T.; Sun, G.; Liu Ai, Q.; Zheludev Nikolay, I.; Tsai Din, P., Magnetic Plasmon Induced Transparency in Three-Dimensional Metamolecules. *Nanophotonics* **2012,** *1*, 131.

65. Knight, M. W.; Wu, Y.; Lassiter, J. B.; Nordlander, P.; Halas, N. J., Substrates Matter: Influence of an Adjacent Dielectric on an Individual Plasmonic Nanoparticle. *Nano Lett.* **2009,** *9*, 2188-2192.

66. Wu, Y.; Nordlander, P., Finite-Difference Time-Domain Modeling of the Optical Properties of Nanoparticles near Dielectric Substrates. *J. Phys. Chem. C* **2010,** *114*, 7302-7307.

67. Chen, Y.; Zhang, Y.; Koenderink, A. F., General Point Dipole Theory for Periodic Metasurfaces: Magnetoelectric Scattering Lattices Coupled to Planar Photonic Structures. *Opt. Express* **2017,** *25*, 21358-21378.

68. Plum, E.; Fedotov, V. A.; Zheludev, N. I., Optical Activity in Extrinsically Chiral Metamaterial. *Appl. Phys. Lett.* **2008,** *93*, 191911.

69. Maoz, B. M.; Ben Moshe, A.; Vestler, D.; Bar-Elli, O.; Markovich, G., Chiroptical Effects in Planar Achiral Plasmonic Oriented Nanohole Arrays. *Nano Lett.* **2012,** *12*, 2357-2361.

70. Tretyakov, S.; Sihvola, A.; Sochava, A.; Simovski, C., Magnetoelectric Interactions in Bi-Anisotropic Media. *J Electromagnet Wave* **1998,** *12*, 481-497.

71. Davis, M. S.; Zhu, W.; Strait, J.; Lee, J. K.; Lezec, H. J.; Blair, S.; Agrawal, A., Chiroptical Response of Aluminum Nanocrescents at Ultraviolet Wavelengths. *Nano Lett.* **2020**.

72. Wakabayashi, M.; Yokojima, S.; Fukaminato, T.; Shiino, K.-i.; Irie, M.; Nakamura, S., Anisotropic Dissymmetry Factor, G: Theoretical Investigation on Single Molecule Chiroptical Spectroscopy. *J. Phys. Chem. A* **2014,** *118*, 5046-5057.

73. Gibbs, J. G.; Mark, A. G.; Eslami, S.; Fischer, P., Plasmonic Nanohelix Metamaterials with Tailorable Giant Circular Dichroism. *Appl. Phys. Lett.* **2013,** *103*, 213101.

74. Esposito, M.; Tasco, V.; Cuscunà, M.; Todisco, F.; Benedetti, A.; Tarantini, I.; Giorgi, M. D.; Sanvitto, D.; Passaseo, A., Nanoscale 3D Chiral Plasmonic Helices with Circular Dichroism at Visible Frequencies. *ACS Photonics* **2015,** *2*, 105-114.

75. Kosters, D.; de Hoogh, A.; Zeijlemaker, H.; Acar, H.; Rotenberg, N.; Kuipers, L., Core–Shell Plasmonic Nanohelices. *ACS Photonics* **2017,** *4*, 1858-1863.

76. Tinder, R. F., *Tensor Properties of Solids: Phenomenological Development of the Tensor Properties of Crystals*. Morgan & Claypool Publishers: San Rafael, California, 2008.

77. Belov, P. A.; Maslovski, S. I.; Simovski, K. R.; Tretyakov, S. A., A Condition Imposed on the Electromagnetic Polarizability of a Bianisotropic Lossless Scatterer. *Tech. Phys. Lett.* **2003,** *29*, 718-720.

78. Sersic, I.; Tuambilangana, C.; Kampfrath, T.; Koenderink, A. F., Magnetoelectric Point Scattering Theory for Metamaterial Scatterers. *Phys. Rev. B: Condens. Matter Mater. Phys.* **2011,** *83*, 245102/245101-245102/245112.

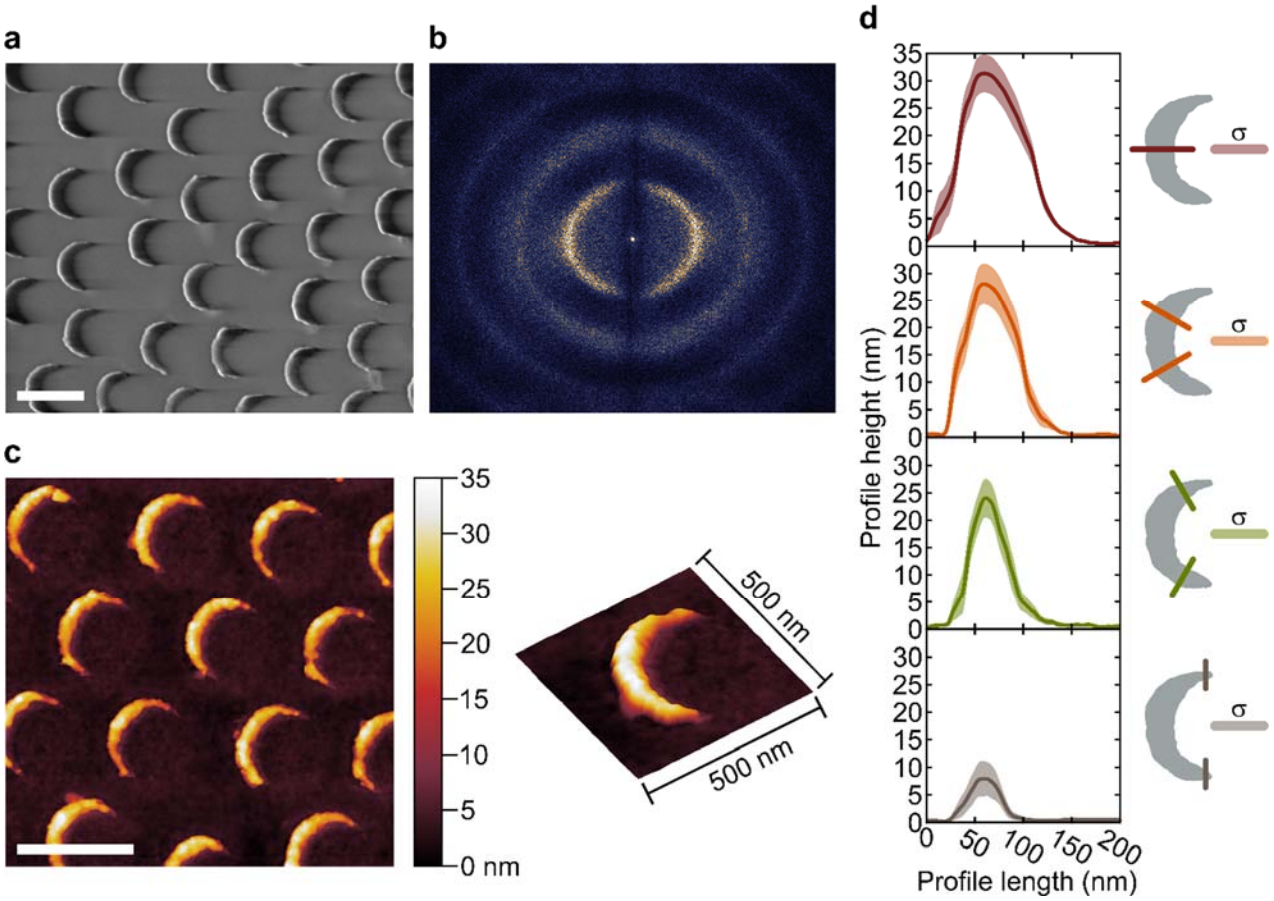

Figure 1. Au NC structural and array features. (a) SEM micrograph, with a 500 nm scale bar, depicting Au NC aspect ratio. (b) Fourier transform image analysis of a 5,000 μm^2 array area (4,000x magnification) illustrating long-range periodicity of the NC array (see Figure S2 for the corresponding SEM micrograph). (c) 2D and 3D AFM micrographs, with 500 nm scale bars, showing Au NC topography. Using AFM data, (d) cross-section profiles were averaged over 100 NC structures from the center mirror plane along the backbone of the NC (red) and at ±30° (orange), ±60° (green), and ±90° (grey) radially off-center from the backbone. Each off-center cross-section profile is calculated by averaging the values at the two indicated locations.

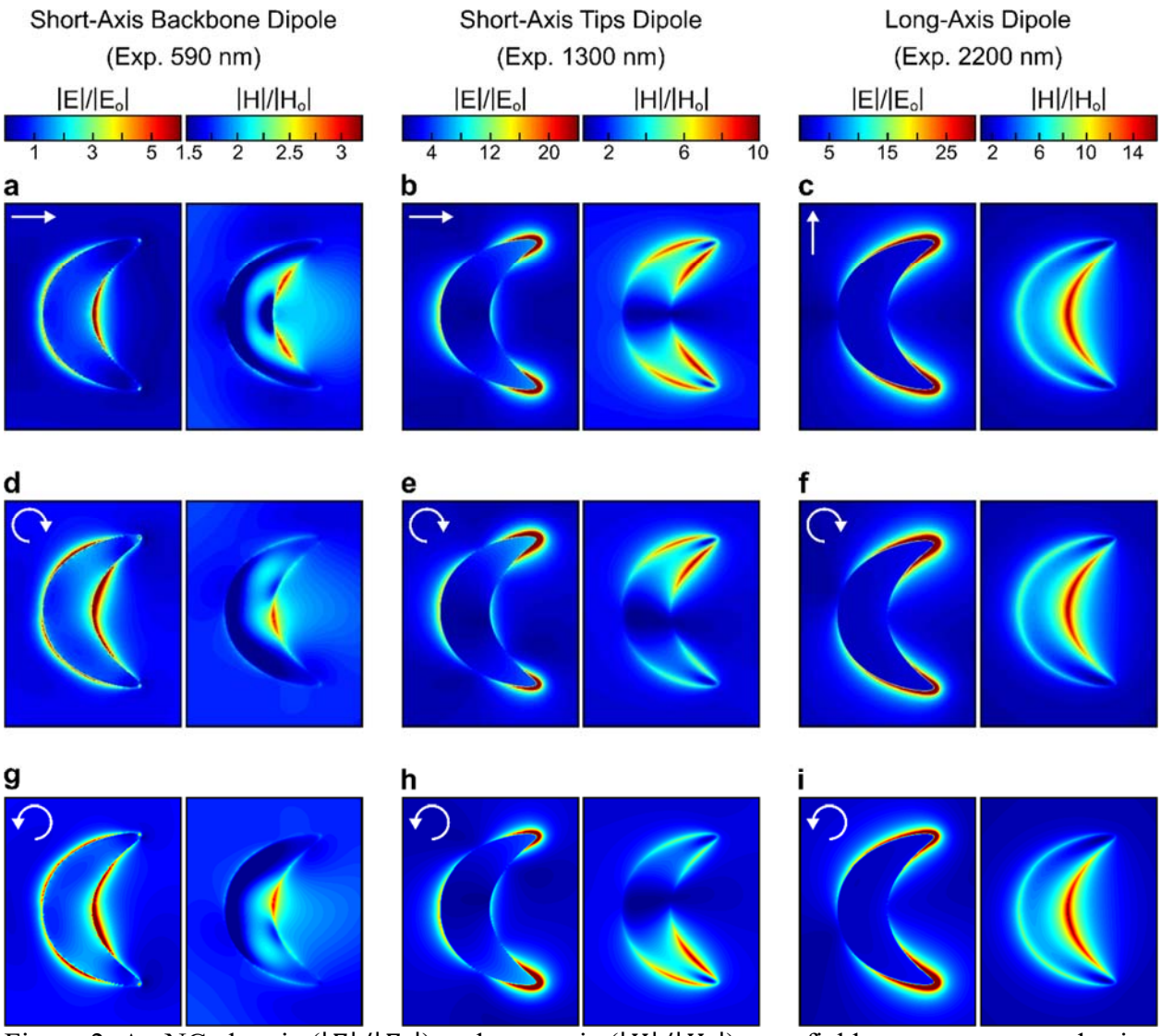

Figure 2. Au NC electric ($|E|/|E_o|$) and magnetic ($|H|/|H_o|$) near-field patterns generated using FDTD calculations. Responses at normal incidence from (a-c) PPL, LCP light (d-f), and RCP light (g-i). In all subfigures, the white arrow indicates the incident polarization. The respective intensity gradient scales pertain to the column of plots below them. These simulated near-field patterns correspond to resonance modes described as a short-axis backbone dipole (a, d, and g), a short-axis tips dipole (b, e, and h), and a long-axis dipole (c, f, and i). Upon comparison of calculated and experimental extinction spectra (see main text and Figure 3), these three dominant resonance modes are respectively assigned to the experimental peaks at 590, 1300, and 2200 nm.

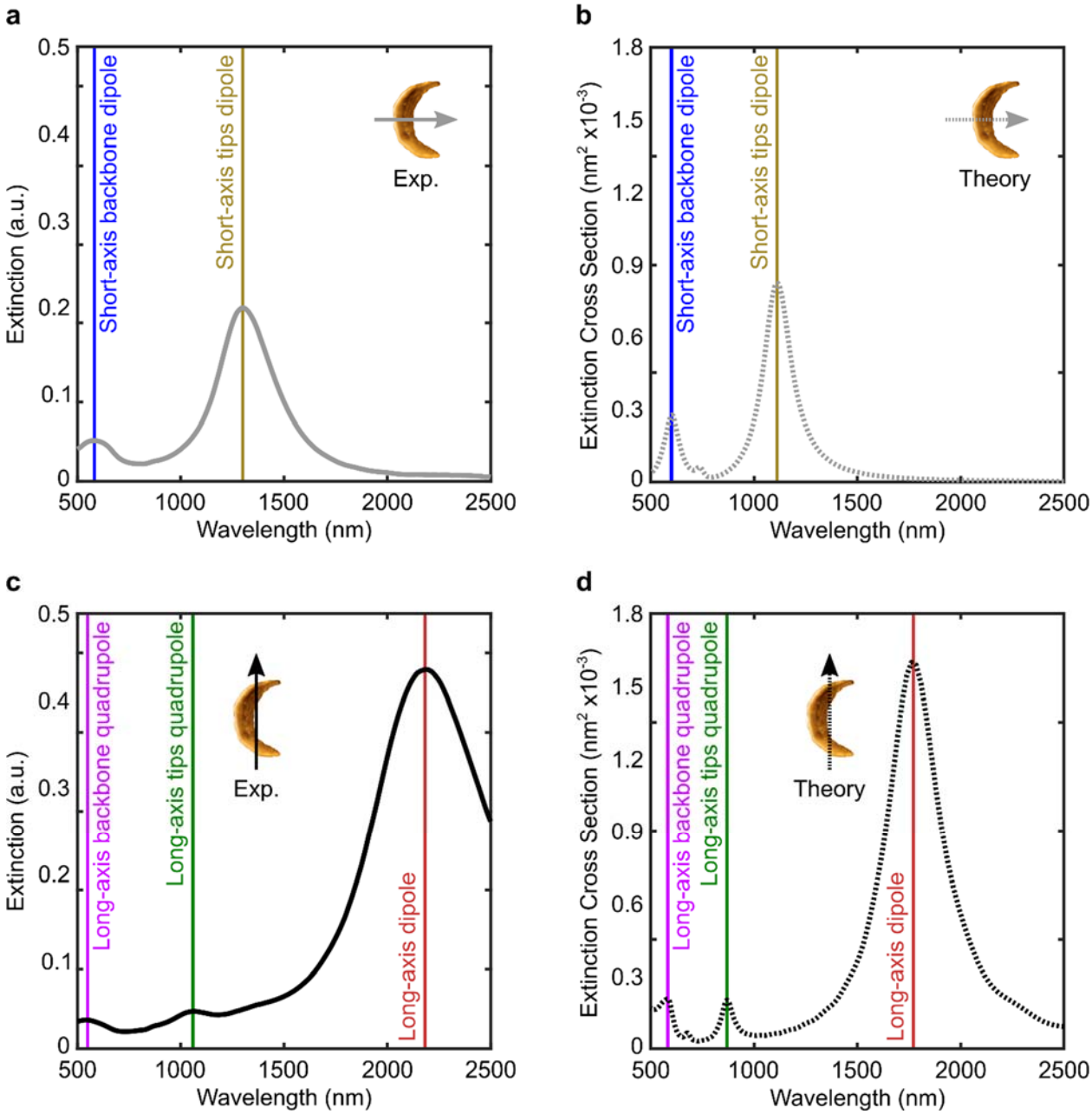

Figure 3. Comparison of experimental and FDTD simulated LSPR optical extinction spectra. The incident PPL is oriented according to the inset arrows and NC orientation shown. (a) Experimental short-axis excitation with resonances at 590 nm and 1300 nm. (b) Theoretical short-axis excitation with resonances at 600 nm and 1100 nm. (c) Experimental long-axis excitation with resonances at 550 nm, 1060 nm, and 2200 nm. (d) Theoretical long-axis excitation with resonances at 580 nm,

870 nm, and 1800 nm. Theoretical calculations are performed using the single Au NC geometric model shown in Figure S4.

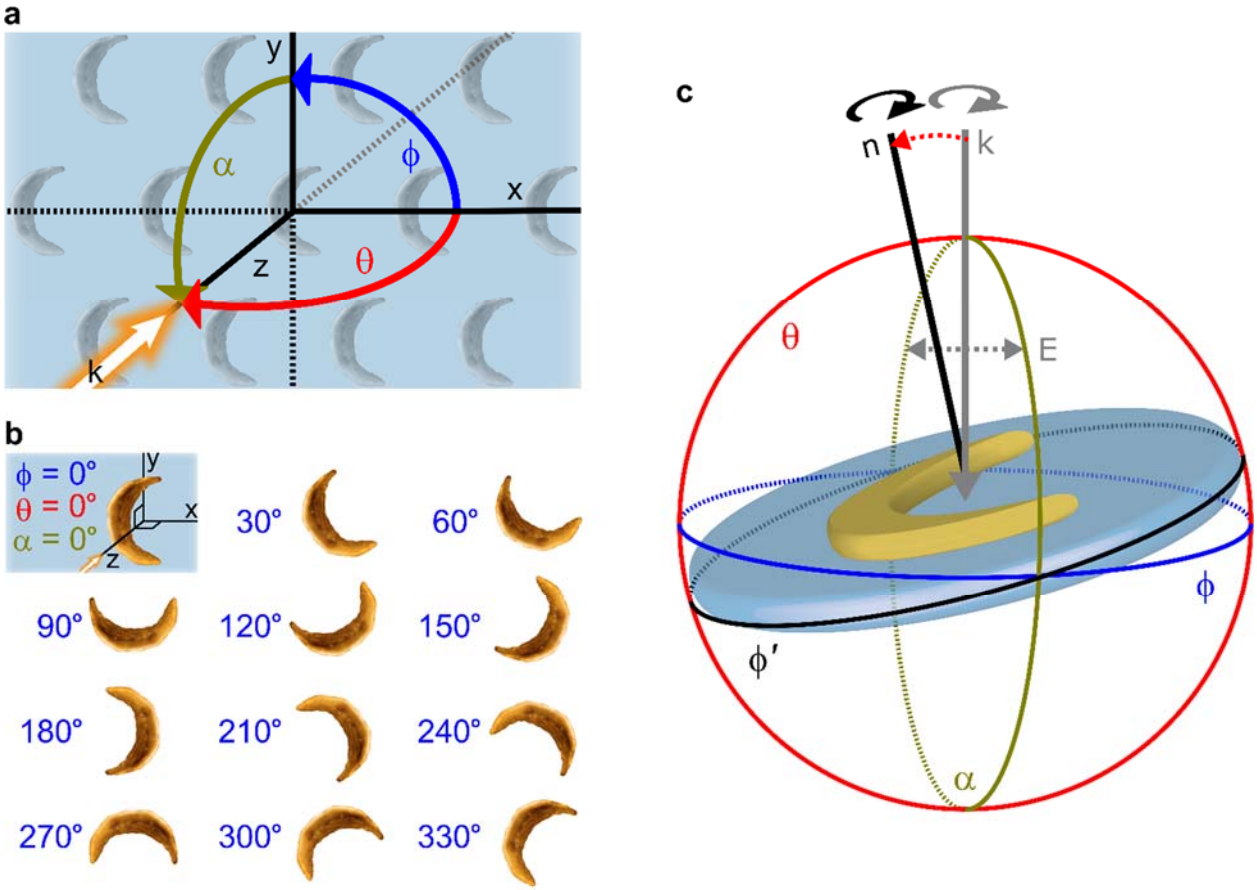

Figure 4. (a) Definitions of NC rotations where the endcap arrow indicates a positive value rotation from the respective starting plane relative to the incident light, k, propagating along the z-axis. Here, the substrate with NC array resides in the xy plane. (b) Reference key for representative in-plane NC rotations by ϕ. (c) Illustration of representative rotations applied in the orientation-dependent extinction experiments depicted in Figures 5, 6, and 9. The illustration in (c) aids visualization of combined *s*- and *p*-polarizations of the incident PPL (grey dashed double arrow) in each associated experiment. The NC substrate is shown tilted from the optical axis to $\theta = 30°$ where the light is *s*-polarized (E-field along y-axis, in the α plane) and remains so as the substrate is rotated around its normal axis, n, by angle ϕ'. This description applies to the experiments of Figures 5 and 9. For the experiments of Figure 6, the substrate is fixed in a given α, θ, ϕ orientation and PPL is rotated by the azimuthal angle ϕ in the laboratory frame (grey circular arrow to indicate

rotation). In this methodological description, incident PPL fluctuates between combinations of *s*- and *p*-polarized light about the tilted substrate orientation.

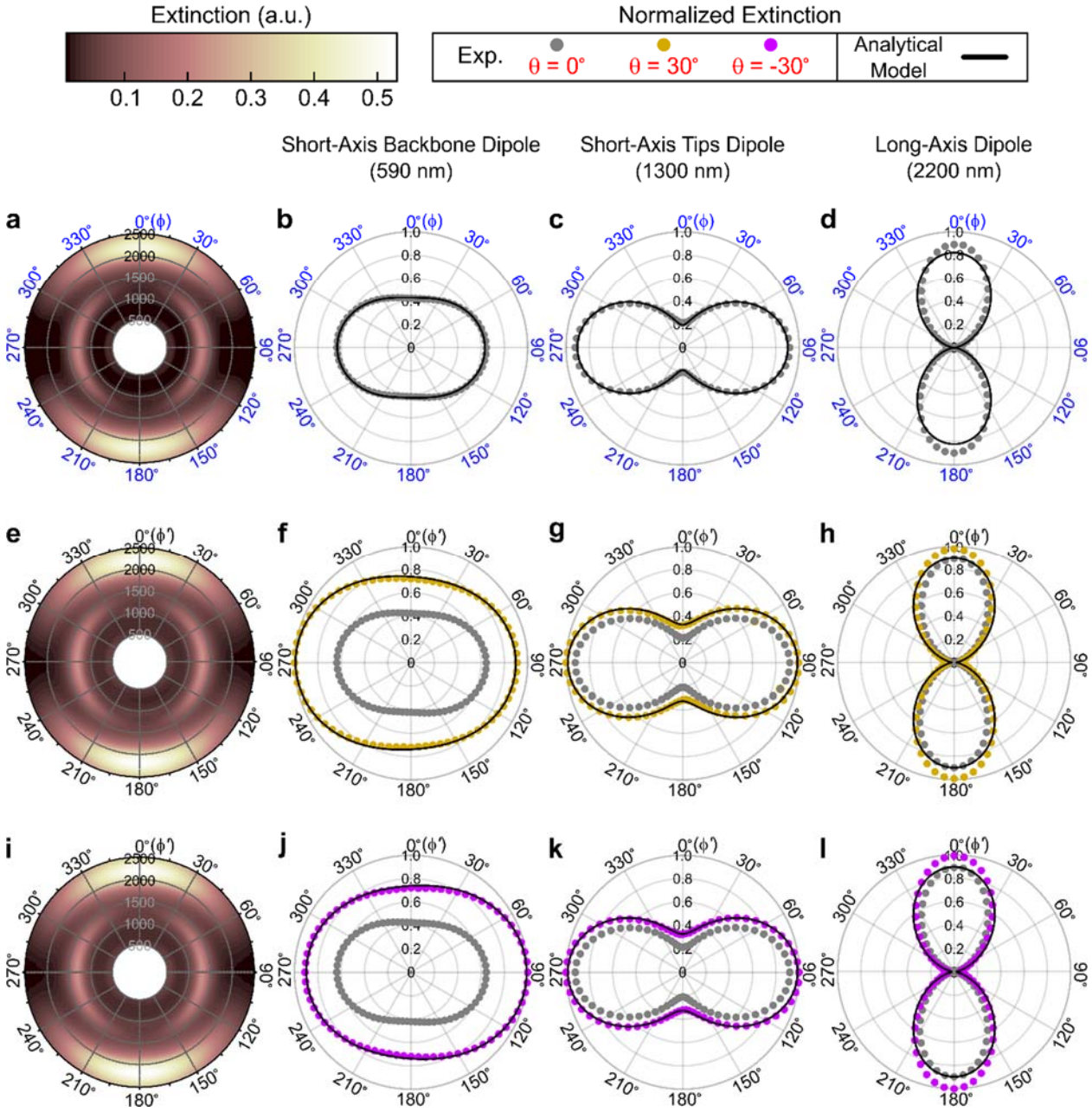

Figure 5. Optical extinction with polarization of light fixed along the vertical y-axis as a function of sample rotation in ϕ (ϕ' for out-of-plane orientations) and θ (see Figure 4; $\alpha = 0°$ throughout). For the polar contour plots at (a) $\theta = 0°$, (e) $\theta = 30°$, and (i) $\theta = -30°$, the radial axis is the wavelength range 500 nm to 2500 nm. Polar plots show respective peak wavelength profiles at designated orientations: (b, f, and j) short-axis backbone dipole mode at 590 nm, (c, g, and k) short-axis tips dipole mode at 1300 nm, and (d, h, and l) long-axis dipole mode at 2200 nm. For θ =

±30° (f-h and j-l), the normal incidence extinction profile (b-d) is inlayed in gray for comparison. Polar plots for peak resonances are normalized within each respective wavelength set. The analytical fits are shown in black.

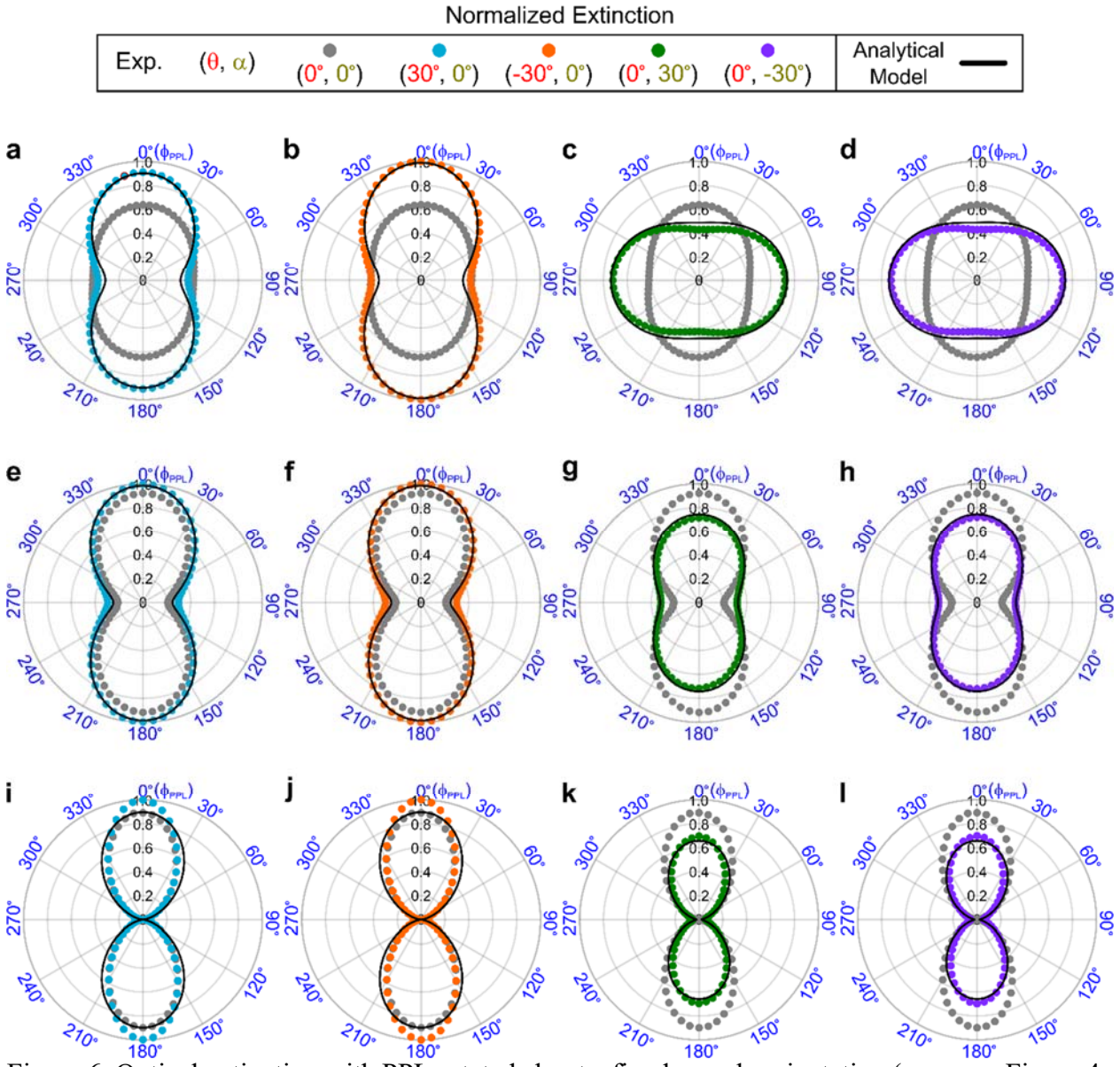

Figure 6. Optical extinction with PPL rotated about a fixed sample orientation (compare Figure 4c where ϕ_{PPL} rotation is proportionate to ϕ in the laboratory frame). Polar plots show respective peak LSPR profiles at designated orientations involving both θ and α. (a-d) Short-axis backbone dipole mode at 590 nm at ϕ = 90°, (e-h) short-axis tips dipole mode at 1300 nm oriented at ϕ = 90°, and (i-l) long-axis dipole mode at 2200 nm oriented at α = 0°. Maxima observed in (c, d) due to selective excitation of the long-axis backbone quadrupole mode. The normal incidence extinction profile (equivalent to Figure 5b-d) is inlayed for comparison. Polar plots for peak

resonances are normalized within each respective wavelength set. The analytical fits are shown in black.

Table 1. Selected optical extinction intensity changes from Figure 6 quantifying the range of active plasmonic character.

Au NC orientation (α, θ)	Short-axis backbone dipole *$(\phi' = 90°)$*	Short-axis tips dipole *$(\phi' = 90°)$*	Long-axis dipole *$(\phi' = 0°)$*
	$\phi_{PPL} = 0°$ (180°)		
(30°, 0°)	0.27[a]	0.08	0.11
(-30 0°)	0.36	0.08	0.11
(0°, 30°)	-0.21[a]	-0.21	-0.20
(0°, -30°)	-0.21	-0.21	-0.20
	$\phi_{PPL} = 90°$ (270°)		
(30°, 0°)	-0.05	0.09	0.05
(-30°, 0°)	-0.01	0.09	0.05
(0°, 30°)	0.30	0.11	0.04
(0°, -30°)	0.30	0.11	0.04

[a] Sign indicates either an increase $(+)$ or a decrease $(-)$ from normal incidence optical extinction intensity.

Figure 7. Graphical representation of polarizability terms relevant for modeling linear (A_{linear}, a.u.) and CD (A_{CD}, a.u.) extinction of (a) long-axis dipole mode at 2200 nm, (b) short-axis tips

dipole mode at 1300 nm, and (c) short-axis backbone dipole mode at 590 nm. The A_{linear} and A_{CD} values are from independent fittings, and values from different fittings cannot be meaningfully compared. To match previous literature convention for such graphical representation,[47] $A_{i,jl}^{FG}$ terms from the fitting model of Equations 4-6 have been doubled for F, $G = E$, H (see Supporting Information). Polarizability elements determined to contribute insignificantly to orientation-dependent extinction and incident polarizations are omitted in the plots (white area); however, these elements may be relevant for other experimental conditions not evaluated in this work.

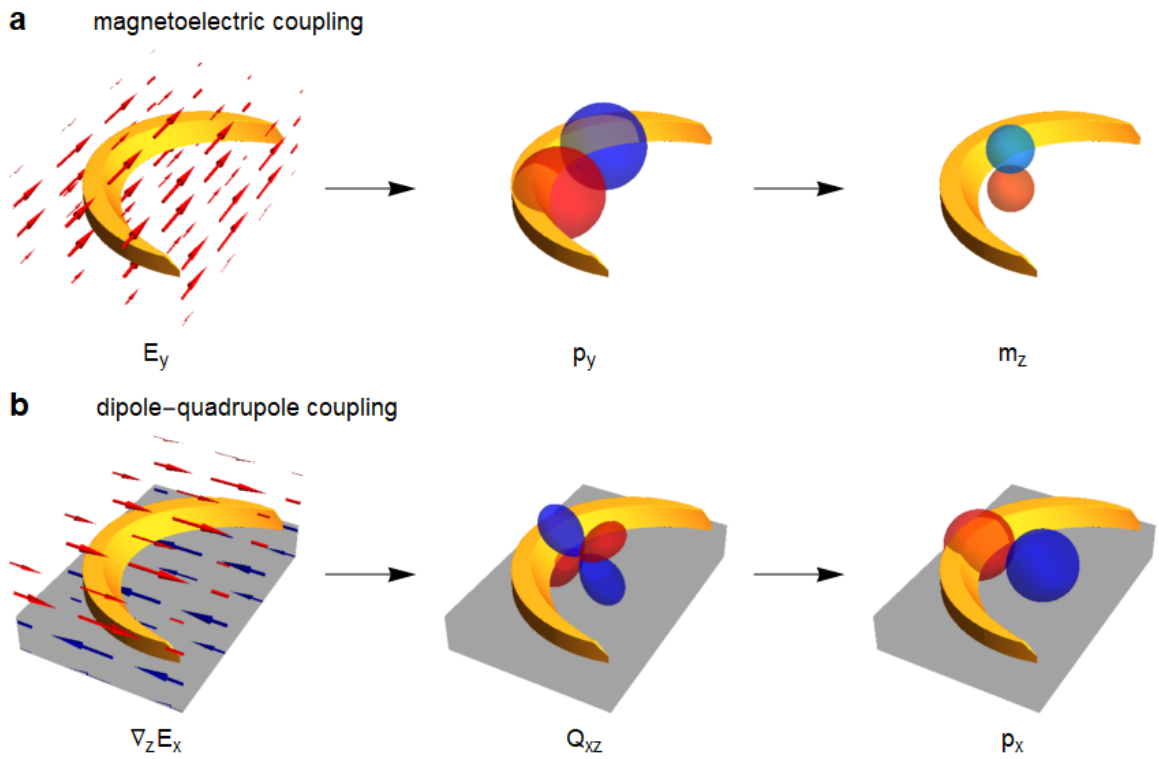

Figure 8. Schematic illustration of representative structure-induced multipole interactions in Au NCs. (a) Magnetoelectric coupling: E_y excites electric dipole p_y, causing charges to circulate the ring-like backbone and thereby exciting magnetic dipole m_z. (b) Dipole-quadrupole coupling: the gradient $\nabla_z E_x$ of the incident E_x-polarized field excites electric quadrupole Q_{xz}. Because the bottom portion of the NC has larger size and greater proximity to the dielectric substrate, the bottom lobes of quadrupole mode dominate the multipolar response, thereby exciting an electric dipole p_x of matching symmetry.

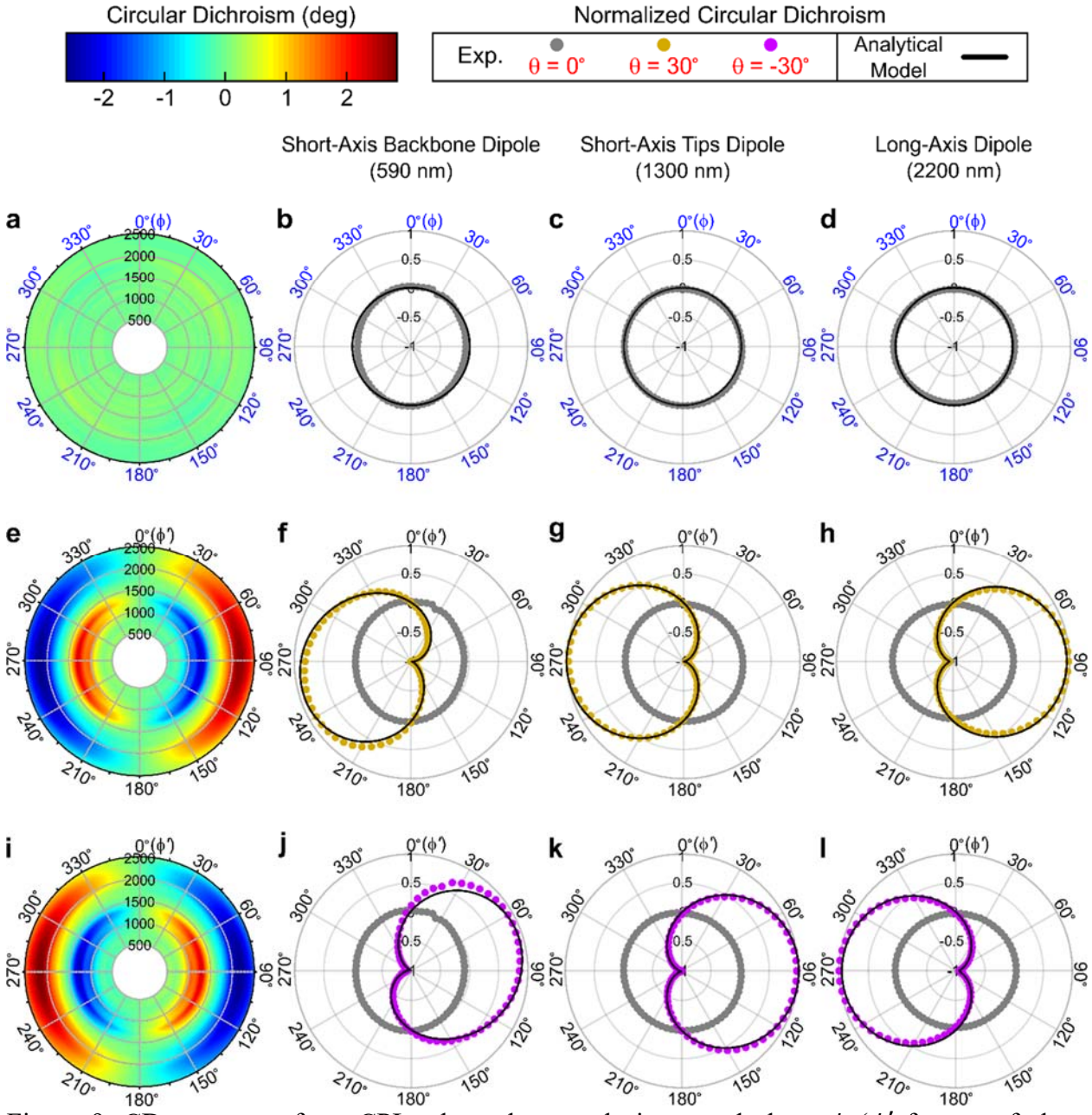

Figure 9. CD responses from CPL where the sample is rotated along ϕ (ϕ' for out-of-plane orientations) and θ (see Figure 4; $\alpha = 0°$ throughout). For the polar contour plots at (a) $\theta = 0°$, (e) $\theta = 30°$, and (i) $\theta = -30°$, the radial axis is the wavelength range 500 nm to 2500 nm. Polar plots show respective peak wavelength CD profiles at designated orientations: (b, f, and j) short-axis backbone dipole mode at 590 nm, (c, g, and k) short-axis tips dipole mode at 1300 nm, and (d, h, and l) long-axis dipole mode at 2200 nm. For $\theta = \pm 30°$ (f-h and j-l), the normal incidence CD

extinction (b-d) is inlayed for comparison. Polar plots for peak resonances are normalized within each respective wavelength set. The analytical fits are shown in black.

Table 2. Anisotropy (g) factors from CD responses in Figure 9 quantifying the range of active chiral plasmonic character ($\alpha = 0°$ throughout).

Sample orientation θ	Short-axis backbone dipole	Short-axis tips dipole	Long-axis dipole
	Au NC at $\phi' = 90°$		
30°	-0.16[a]	-0.55	0.44
-30°	0.12	0.55	-0.44
	Au NC at $\phi' = 270°$		
30°	0.12	0.55	-0.44
-30°	-0.16	-0.55	0.44

[a] Sign indicates $(+)$ left- or $(-)$ right-handedness at designated orientations.

For Table of Contents Only